

See discussions, stats, and author profiles for this publication at: <https://www.researchgate.net/publication/324269535>

Optimization for Gold Nanostructure-Based Surface Plasmon Biosensors Using a Microgenetic Algorithm

Article in ACS Photonics · April 2018

DOI: 10.1021/acspolitcs.8b00136

CITATIONS

4

READS

318

5 authors, including:



Po-Han Fu

Academia Sinica

18 PUBLICATIONS 217 CITATIONS

[SEE PROFILE](#)



Shu Cheng Lo

National Taiwan University

6 PUBLICATIONS 8 CITATIONS

[SEE PROFILE](#)



Po Cheng Tsai

National Taiwan University

5 PUBLICATIONS 10 CITATIONS

[SEE PROFILE](#)



Kuang-Li Lee

Academia Sinica

66 PUBLICATIONS 944 CITATIONS

[SEE PROFILE](#)

Some of the authors of this publication are also working on these related projects:



Biosensors [View project](#)

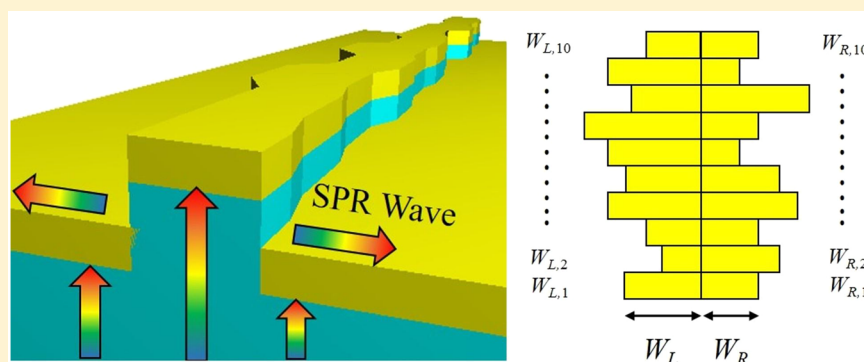
Optimization for Gold Nanostructure-Based Surface Plasmon Biosensors Using a Microgenetic Algorithm

Po-Han Fu,[†] Shu-Cheng Lo,[†] Po-Cheng Tsai,[†] Kuang-Li Lee,[†] and Pei-Kuen Wei^{*,†,‡,§}

[†]Research Center for Applied Sciences, Academia Sinica, Taipei 11529, Taiwan

[‡]Institute of Optoelectronic Sciences, National Taiwan Ocean University, Keelung 20224, Taiwan

[§]Institute of Biophotonics, National Yang-Ming University, Taipei 11221, Taiwan



ABSTRACT: We present a design method and fabrication technique for enhancing detection sensitivity of gold nanostructure-based surface plasmon resonance (SPR) biosensors. In this case, the nanostructure geometry is arbitrary and the optimal design parameters are determined using a microgenetic algorithm integrated with three-dimensional finite-difference time-domain (3D-FDTD) electromagnetic simulations. The corresponding device is fabricated using hot embossing nanoimprint lithography. Two experimental configurations are used to evaluate the device performance: one is the atomic layer deposition and the other is the protein–protein interaction. The performances of the optimal SPR biosensors are superior to the ones with conventional simple structures under both configurations. The improvements in terms of the fitness function are respectively up to 179% and 128% for the 3D-FDTD simulation and the experimental results. The calculated optical fields indicate that the improvement of the fitness function results from the enhancement of localized SPR at the edges of gold nanostructures.

KEYWORDS: biosensor, genetic algorithm, nanostructure, optimization, surface plasmon

Over the decades, the surface plasmon resonance (SPR) sensing technique has drawn intensive research interest for various applications including medical diagnostics, environmental monitoring, and food safety owing to the feature of real-time and label-free detection with high sensitivity.^{1–3} One of the most common methods using a prism for SPR wave excitation is known as the Kretschmann configuration,^{1,4} where the propagation constants of the obliquely incident light and the SPR wave should be matched. In addition to the Kretschmann configuration, periodic metallic nanostructures provide an additional lattice momentum for phase matching so that the SPR wave can be generated by normal incidence. A periodic nanostructure-based SPR sensor has a small detection volume and no need for a prism. Owing to the facility of the experimental setup, periodic metallic nanostructures have been utilized for biodetection.^{5–17} The SPR on the periodic metallic surface is known as Bloch-wave surface plasmon polarization (BW-SPP). For normal incidence, the dispersion relation of the BW-SPP for a one-dimensional metallic grating is governed by¹

$$\frac{2\pi}{\lambda_{\text{SPR}}} \sqrt{\frac{\epsilon_m n^2}{\epsilon_m + n^2}} = \frac{2\pi m}{P} \quad (1)$$

where λ_{SPR} is the corresponding resonant wavelength, ϵ_m and n are respectively the metal permittivity and effective surface refractive index, m is the diffraction order, and P is the grating periodicity. Note that the biomolecular thickness is usually much smaller than the evanescent length of the surface plasmon field. As shown in Figure 1, the effective index change Δn_{eff} can be approximated by

$$\Delta n_{\text{eff}} = (n_a - n_s) \left[1 - \exp\left(\frac{-2t}{l_d}\right) \right] \quad (2)$$

where n_a is the adsorbate bilayer (adlayer) refractive index, n_s is the refractive index of the bulk solution, t is the thickness of the adlayer, and l_d is the decay length of the evanescent field (where the amplitude drops to $1/e$). When the biomolecular

Received: February 2, 2018

Published: April 6, 2018

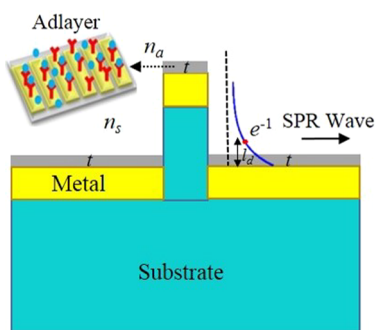


Figure 1. Schematic of an SPR biosensor with the adlayer.

thickness and refractive indices of the solution and adlayer are known, the SPR sensitivity is determined by resonant quality and the evanescent length. The usual evanescent length of the propagating SPR is around 200–300 nm. The length is shortened to tens of nanometers when the SPR is localized in a small region. The localized SPR (LSPR) can be formed by metallic nanoparticles, holes, or sharp edges. However, the LSPR exhibits a much wider resonant line width than the BW-SPP. There is a trade-off between the evanescent length and resonant quality.

In this paper, we propose increased LSPR effects in periodic gold-capped nanostructures by introducing a nanometer irregularity in the nanostructures. Such a configuration reduces the effective evanescent length. The nanostructures are segmented into several discrete sections where the width and position of every section is arbitrary and the geometry is eventually determined using the genetic algorithms (GAs). GAs are the optimization techniques based on the principle of natural selection. GAs are highly effective in handling the problem with a high dimensional variable search space, and the solution is not easy to predict based on the knowledge of basic disciplines (i.e., electromagnetics).^{18,19} In addition, GAs exhibit the flexibility that the fitness function for evaluation can be customized for different design principles. In recent years, GAs have been widely used for the optimization of photonic devices,^{19–26} which are shown to be cost-effective in terms of time. However, three-dimensional (3D) simulations are required in this case since the geometry of a SPR biosensor is not infinite in all x , y , and z axes, which may be time-consuming if a classical simple GA (s-GA) with a large number of individuals (e.g., >100) is used. To address this issue, a micro-GA (μ -GA) is an alternative that is suitable for a problem involving 3D simulations. The μ -GAs use a small population of only five individuals that allows for the evaluation of the entire generation by parallel computing with four CPUs. In addition, the μ -GAs reduce the total elapsed time to obtain the optimal solution compared with s-GAs owing to the reduction of the number of total function evaluations.²⁷ We demonstrate the design and fabrication of gold nanostructure-based SPR biosensors. The optimal design parameter is determined using a μ -GA integrated with 3D finite-difference time-domain (FDTD) simulations, and the resultant device is fabricated using hot embossing nanoimprint lithography.²⁸ The result shows that the performance of an SPR sensor is improved if more degrees of freedom are enabled. The improvement of the fitness function is up to 179% and 128% for the optimal design compared with the conventional design for the FDTD simulation and the experiments, respectively.

RESULTS AND DISCUSSION

Capped Gold Nanostructure-Based SPR Biosensors. Figure 2a shows the general view of a gold nanostructure-based

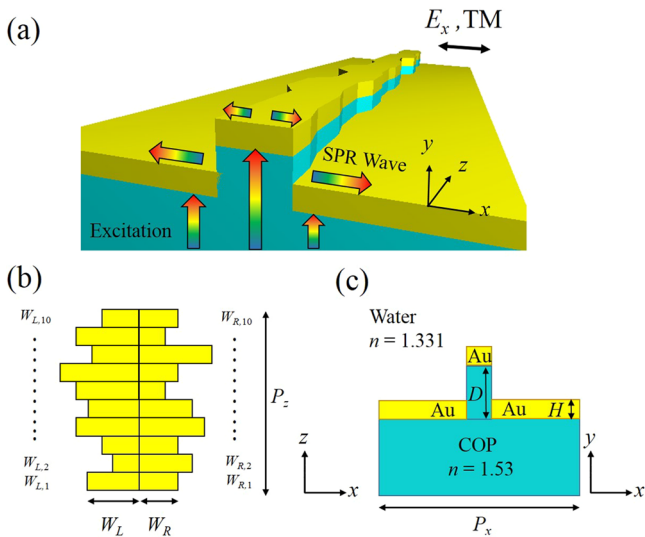


Figure 2. (a) General view of a gold nanostructure-based SPR biosensor in one period. (b) x – z cross-sectional view of capped gold nanostructures. (c) x – y cross-sectional view of the device at a specific value of z .

SPR biosensor in one period. Light is normally incident in the y -direction from the bottom of cyclic olefin polymer (COP) substrate, and the generated SPR wave propagates in the x -direction. The incident electric field E_x is oriented in the x -direction, which is typically defined as TM polarization, and the plasmon field E_y is in the y -direction. The x – z cross-sectional view of the capped gold nanostructure for $-\frac{P_z}{2} < z < \frac{P_z}{2}$ is shown in Figure 2b, where P_z is the periodicity in the z -direction. The structure geometry is segmented into k discrete sections, and $W_{L,i}$ and $W_{R,i}$ represent the left and right boundaries for the i th section (for $i = 1, 2, \dots, k$). Therefore, the width and central position for every section can be determined in this way. The x – z cross-sectional view of the device at a specific value of y is shown in Figure 2c, where P , D , and H represent the grating periodicity in the x -direction, the cap height, and the gold thickness, respectively. The refractive indices of COP and water are 1.53 and 1.331, respectively, and the material dispersion relation of gold used in the following simulations are given in ref 29.

Since the geometry of an SPR biosensor varies in all x , y , and z axes, a 3D simulation is required. In addition, a broadband spectral response is required to evaluate the device performance. In this case, the FDTD method is effective in terms of time because one can obtain the spectral response using a Fourier transform after solving the time domain response at a specific incident wavelength. The following optimization is performed by integrating our in-house-developed μ -GA with the commercial software R-Soft Fullwave for 3D-FDTD electromagnetic simulations.

Microgenetic Algorithm. Consider an SPR sensor as shown in Figure 2 with $P = 500$ nm, $P_z = 1360$ nm, and each period in the y -direction segmented into 10 sections (i.e., $K = 10$). Based on the approximation using eq 1, by choosing $P = 500$ nm, the transmission peak wavelength λ_p is around 670–

690 nm for normal incidence. Also, P_z is chosen to be around $2\lambda_p$ to ensure an effective interaction between the SPR mode and the grating. In this case, only P and P_z are kept constant, while $W_{L,i}$, $W_{R,i}$, D , and H are variables (genes) to be optimized by a μ -GA. Therefore, the design of an SPR sensor can be expressed by a possible solution (individual) \vec{V} containing 22 variables.

$$\vec{V} = [W_{L,1} W_{L,2} \dots W_{L,10} W_{R,1} W_{R,2} \dots W_{R,10} DH] \quad (3)$$

The grid size $\Delta x \times \Delta y \times \Delta z$ is $10 \times 5 \times 17$ nm³ for 3D-FDTD simulations, and all of the variables are multiples of 10 nm to facilitate mesh generation and to ensure the accuracy as well. The domain for $W_{L,i}$ and $W_{R,i}$ is [20 nm, 70 nm] to ensure that the width of a grating is not less than 40 nm, which is the line width limitation of electron-beam (e-beam) lithography. On the other hand, the domains for D and H are [40 nm, 120 nm] and [20 nm 70 nm], respectively.

In a μ -GA, a specific function (fitness function) is required to evaluate the performance of each individual. The performance of the device can be evaluated in terms of several combined factors such as the peak wavelength shift,¹³ distortion of the transmission lobe,³⁰ intensity change at a specific wavelength without and with the adlayer,³¹ etc. By considering the effects of the resonant quality and wavelength shift, we used the spectral integration analysis (SIA) as the fitness function. The SIA considers all absolute intensity changes in the entire SPR spectrum. This analysis is sensitive to the spectral shift and resonant quality. It greatly enhances the signal-to-noise ratios and improves the detection limit. The SIA methods have been conducted for the analysis of other nanostructures, including nanohole SPR sensors and Fano resonances in nanoslit sensors.^{32,33} The fitness function F based on the SIA is the summation of the absolute values of the differences between $S(\lambda)$ and $S_0(\lambda)$ for $\lambda_1 < \lambda < \lambda_2$, which is expressed as

$$F = \sum_{\lambda=\lambda_1}^{\lambda_2} |S(\lambda) - S_0(\lambda)| \quad (4)$$

where $S(\lambda)$ and $S_0(\lambda)$ are respectively the transmission spectra of a SPR sensor before and after the interactions between bovine serum albumin (BSA) and anti-BSA. The thickness of the BSA–anti-BSA adlayer is 5 nm, and the refractive index of BSA is given in ref 34. Based on the definition of F , the optimal solution is expected to exhibit an abrupt shape distortion and peak shift as well. In addition, we choose $\lambda_1 = 650$ nm and $\lambda_2 = 720$ nm to ensure that the range $[\lambda_1, \lambda_2]$ covers the whole transmission lobe of an SPR mode.

Figure 3 shows the flowchart of the optimization process for an SPR biosensor using a μ -GA. The μ -GA begins once the initial population emerges, which is five for each generation. One of the individuals (designs) among the initial population is determined, which is assigned to be the optimal design in this framework where $D = 90$ nm, $H = 50$ nm, and $W_{L,i} = W_{R,i} = 30$ nm for all i . On the other hand, the remaining four individuals are randomly generated in the search space. Note that the initial population can be any reasonable design that can be fabricated using hot embossing nanoimprint lithography. Therefore, a typical case is chosen for the initial population, and it is a proper benchmark for the following comparison where the final optimized design should be by no means inferior to the initial design under any definitions of F . The corresponding F values for five individuals are calculated then a selection operator is used. The fittest individual (elite) is directly carried to the next

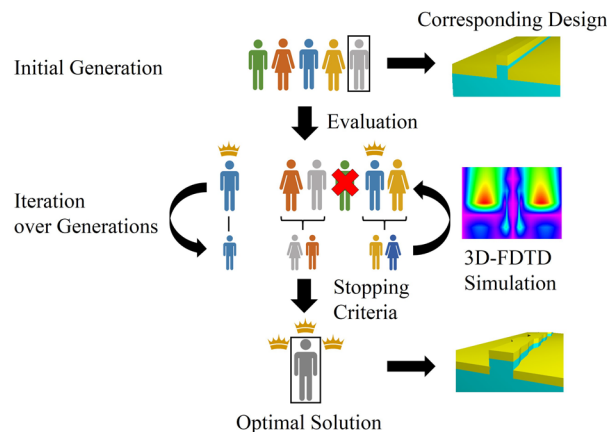


Figure 3. Flowchart of an optimization process for an SPR biosensor using a μ -GA.

generation, while the worst individual is eliminated. The elite and the remaining three individuals are randomly separated into two groups. Each group represents a pair of parents that generate two children (offspring) for the next generation using the single-point crossover method.¹⁸ Note that the mutation operator is not necessary for a μ -GA because enough diversity has already been introduced.²⁷

The problem is evolved toward better designs over the generations, and the μ -GA stops when the evolution reaches 500 generations. During the optimization process, if the improvement of the best fitness value is less than 5% over 20 successive generations, only the fittest individual is kept, while the other four individuals are regenerated randomly. Figure 4a

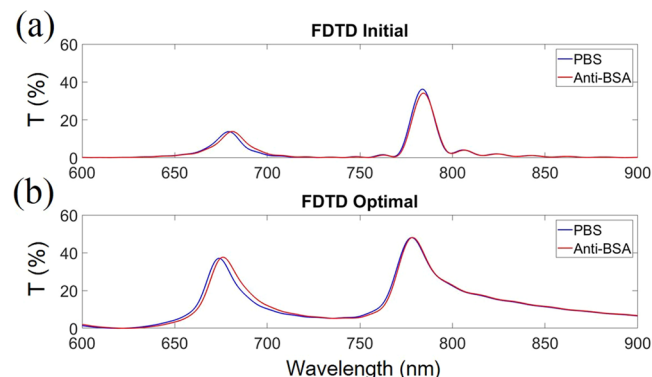


Figure 4. (a) Transmission spectra for the initial and (b) optimal design of PBS cleaning and anti-BSA adsorption.

and b respectively show the transmission spectra (T) for the initial and optimal designs calculated by the 3D-FDTD method. PBS labeled in the legends is the abbreviation of phosphate-buffered saline, which is used for gold surface cleaning. The improvement of F for the optimal design is up to 179% compared with the initial design, and the optimal \vec{V} is shown in Table 1 where $D = 80$ nm and $H = 30$ nm.

The plasmonic field (E_y) distribution at the resonant wavelength λ_{SPR} is required for further investigation for SPR biosensors. Figure 5a and b respectively show the schematics of the capped nanostructures with E_y distributions at λ_{SPR} in x – y cross-sectional views for initial and optimal designs at $z = 0$. For the initial design, the E_y distribution at the upper surface (surface BW-SPP mode) is much stronger than the lower

Table 1. Optimal \vec{V} of the SPR Biosensor

i	$W_{L,i}$ (nm)	$W_{R,i}$ (nm)
1	50	30
2	40	60
3	60	20
4	50	60
5	60	20
6	50	40
7	30	40
8	70	40
9	50	20
10	60	30

surface (substrate BW-SPP mode), and the field decays in the y -direction away from the gold layer, while E_y is weak at the upper surface of the capped nanostructures. In Figure 5b, the optimal device also exhibits similar characteristics for both sides next to the capped nanostructures, whereas one can observe that much stronger fields concentrate at the edges and corners of the capped nanostructures with extremely short decay lengths, which are known as the localized surface plasmons (LSPs). In general, the red-shift occurs once the analytes are immobilized either on the smooth part or at the edges and corners, which can be illustrated by the effects of the BW-SPPs

and LSPs, respectively. For the optimal device, the analytes immobilized at the edges with strong LSPs may contribute to a particularly obvious red-shift owing to the increase of the effective refractive indices of SPR modes. The overall response we care about results from the combined effects including the LSPs and BW-SPPs.

One may wonder whether any solutions in the search space may exhibit satisfactory results because it is well known that E_y tends to concentrate at the edges of the metals based on Maxwell's equations in which the normal displacement of the electric field is continuous at gold/water interfaces. Thus, we generated a random solution for comparison. The capped nanostructure geometry is randomly generated in the search space, while D and H are respectively assigned to be 80 and 30 nm, which are identical to the optimal design. Figure 5c shows the schematic of the randomized capped nanostructures with the E_y distribution at λ_{SPR} in an x - y cross-sectional view, and the resultant transmission spectrum is shown in Figure 6. The improvement of F is 72%, which is far inferior to the optimal design.

We present E_y distributions at λ_{SPR} in the x - z cross-sectional views for further clarification. Figure 7a, b, and c respectively show E_y distributions for initial, optimal, and random designs at the upper surfaces of the capped nanostructures, and the summation and standard deviation of the power flow for -0.25

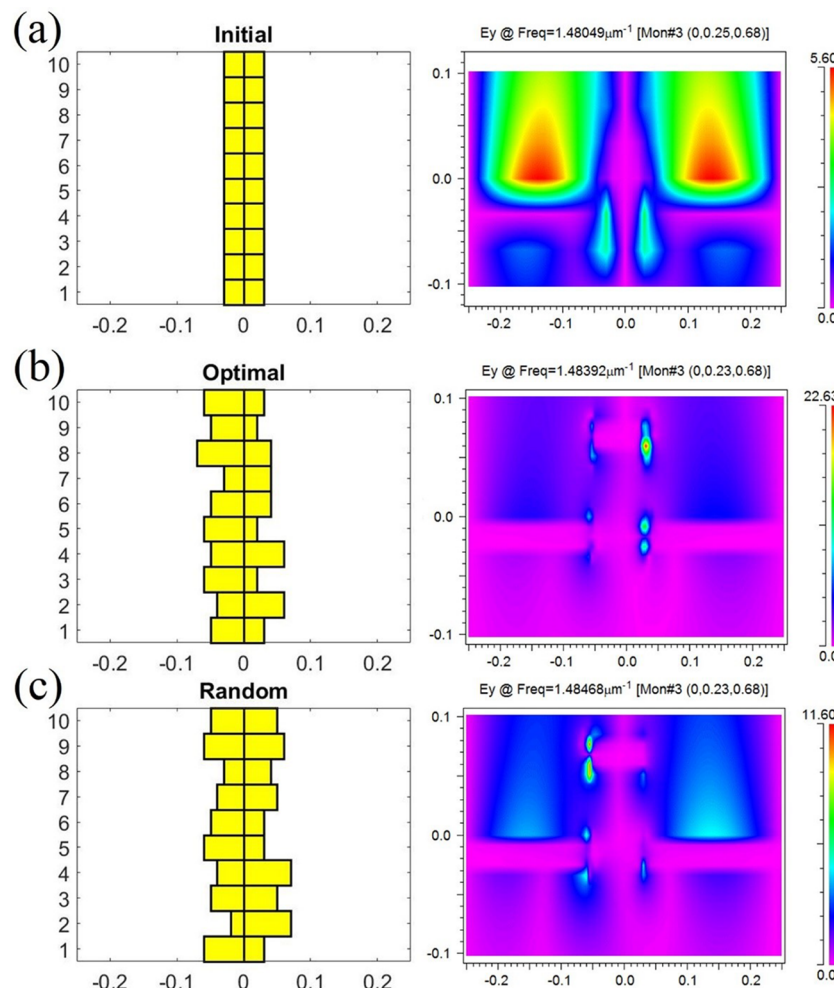


Figure 5. (a) Schematics of capped nanostructures and E_y distributions at λ_{SPR} in the x - y cross-sectional views for the initial and (b) optimal and (c) random designs at $z = 0$.

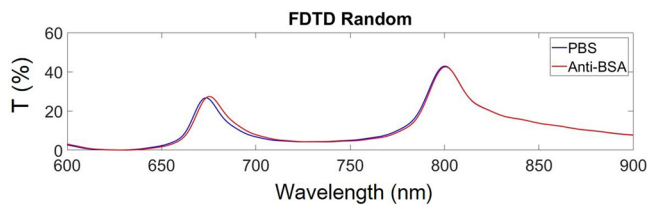


Figure 6. Transmission spectra for randomly designed SPR biosensors of PBS cleaning and anti-BSA adsorption.

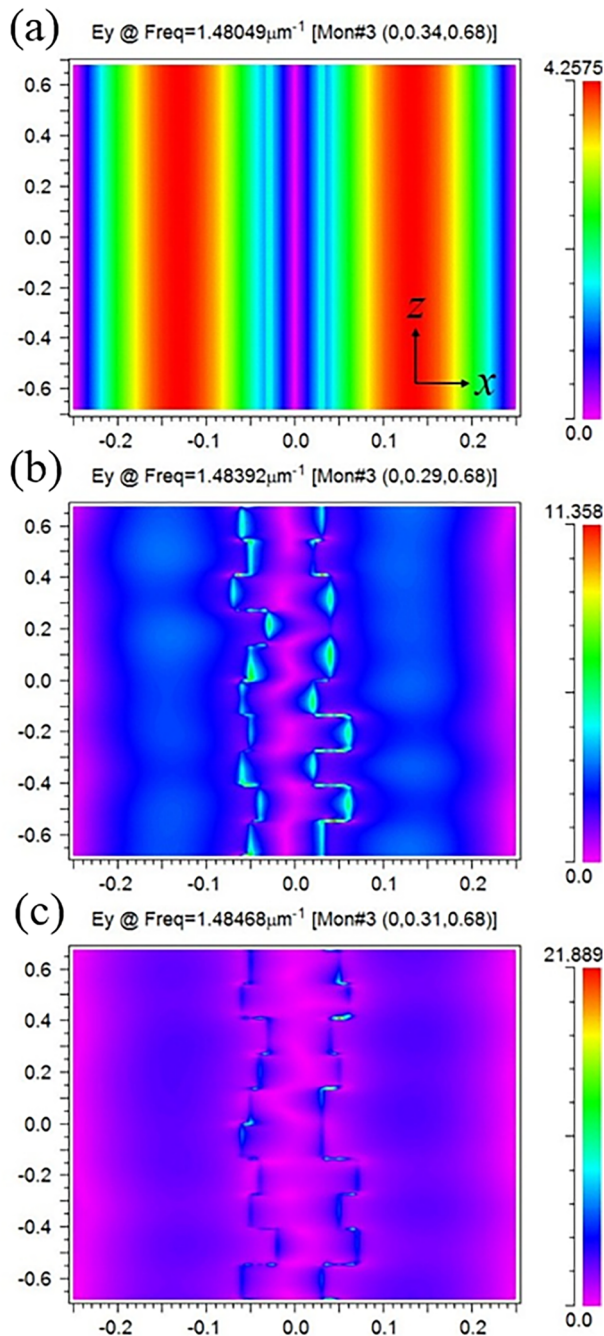


Figure 7. (a) E_y distributions at λ_{SPR} in the x - z cross-sectional views for the initial, (b) optimal, and (c) random designs at the upper surfaces of the capped nanostructures.

$< x < 0.25 \mu\text{m}$ are shown in Figure 8a and b, respectively. For the conventional design, the width and height of the capped

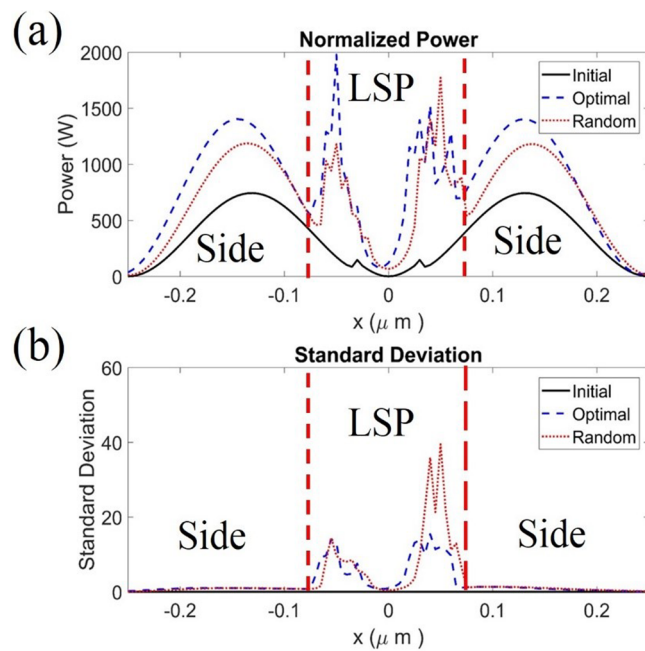


Figure 8. (a) Summation and (b) standard deviation of the power flow for $-0.25 < x < 0.25 \mu\text{m}$.

nanoslit does not play an important role because E_y is weak on the upper surfaces of the capped nanostructures. Thus, the improvement of F is limited if the degrees of freedom are restricted only for the width and height. On the other hand, the LSPs are both strong for optimal and random designs whereas with different distributions. The optimal design exhibits more uniform “hotspots” at the edges along with greater total power for both LSP (central region) and the BW-SPP (side region) compared with the random design and thus with superior performance. In addition, the total near-field power covering the region within 10 nm counting from the top of the gold layer is calculated. Compared with the conventional design, the increase of the total near-field power is 114% and 67% for the optimized and random design, respectively. Note that the redshift is dependent on not only the power magnitude but the distribution as well.

Experimental Section. Figure 9 shows the flowchart of the fabrication process for SPR biosensors using hot embossing nanoimprint lithography. Figure 10a and b respectively show the top-view scanning electron microscope (SEM) images of the nanoslit arrays of the initial and optimal designs, where the dimensions of the nanostructures are close to the design parameters. Two configurations are used for the comparisons of SPR sensing performance: one is the atomic layer (ALD) deposition and the other is the protein–protein (BSA–anti-BSA) interaction.¹³ For the ALD deposition (Syskey Technology Co., LTD), the thickness of the Al_2O_3 layer is 5 nm. On the other hand, for the protein–protein interaction, the concentrations of BSA and anti-BSA (Sigma-Aldrich) are 1 mg/mL and 50 $\mu\text{g}/\text{mL}$, respectively.

For the ALD system, the Al_2O_3 layer is normally deposited on the gold surface using an electron-beam evaporator, and it is more likely to form a thin layer, which is similar to the simulation model. On the other hand, for the BSA–anti-BSA system, it is difficult to predict the distribution by injecting a BSA/anti-BSA solution into a microfluidic channel. Similar to

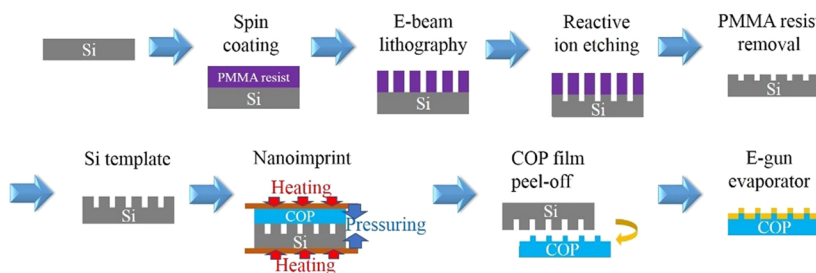


Figure 9. Flowchart of the fabrication process for SPR biosensors.

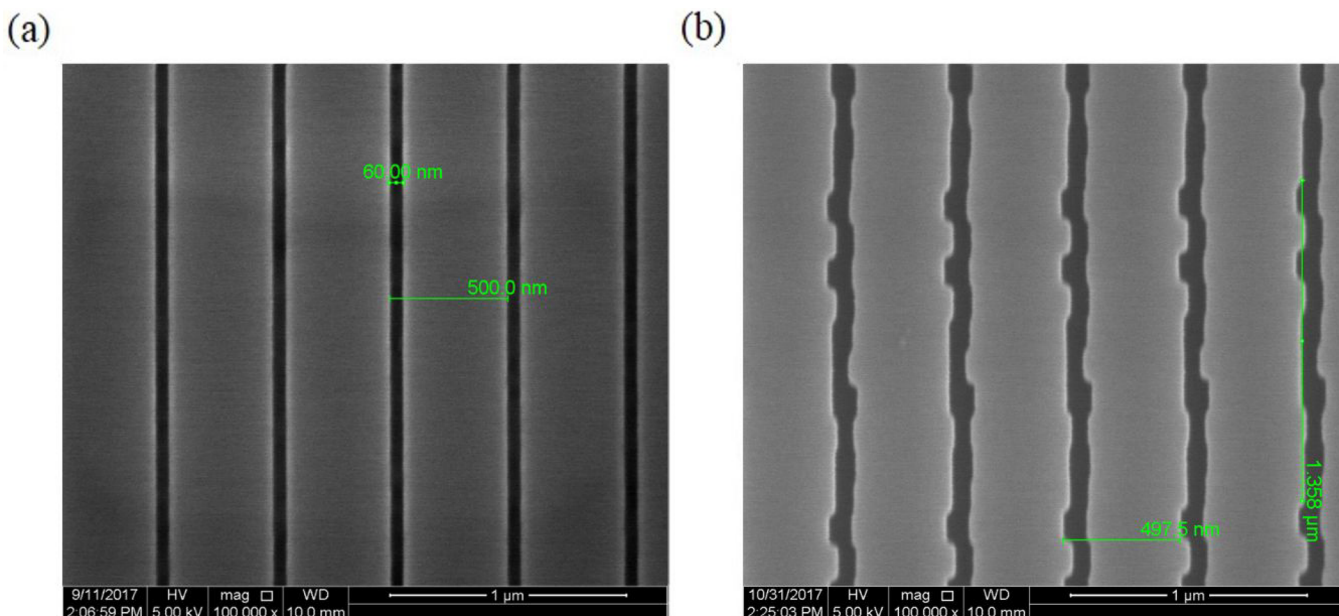


Figure 10. (a) Top-view SEM images of the nanoslit arrays for the initial and (b) optimal designs.

ALD deposition, the BSA–anti-BSA layer tends to adsorb on the top surface of the device for most situations.³⁵

Figures 11 and 12 respectively show the spectral responses before and after the ALD deposition and BSA–anti-BSA interactions. The results of both experimental configurations show consistency as well as good agreements with the 3D-FDTD simulations, and the improvements of F are 128% and 125% compared with the initial design, respectively. The nanometer irregularity induces increased LSPs, which exhibit

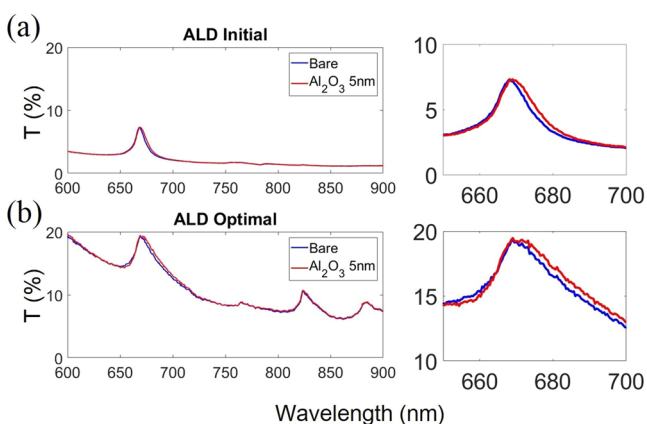


Figure 11. (a) Transmission spectra for the initial and (b) optimal SPR biosensors before and after ALD deposition.

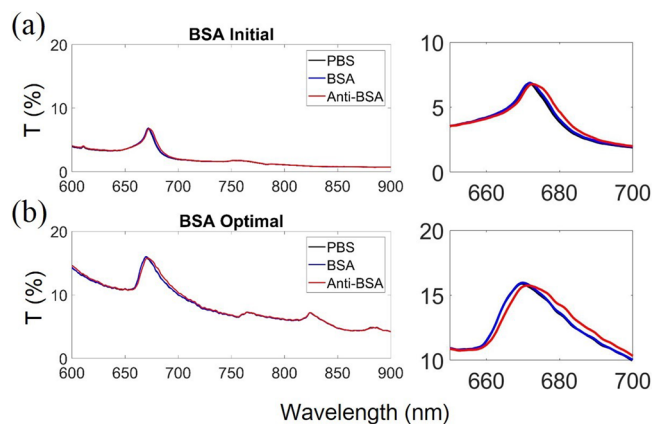


Figure 12. (a) Transmission spectra for the initial and (b) optimal SPR biosensors for PBS cleaning, BSA, and anti-BSA adsorption.

much shorter decay lengths of the evanescent field than that of the SPR mode. Therefore, the thickness sensitivity for thin bilayers is enhanced. The spectra for optimized cases show some ripples that indicate evidence of the LSPs.

The difference between the simulations and experiments stems from the fabrication errors using an e-beam writer. In the simulation models, the gold nanostructures are ideally rectangular with sharp edges at the corners. However, as shown in the scanning microscope image, the corners of the

gold nanostructure are not exactly sharp but have small round fillets due to the fact that the e-beam writer has a resolution limitation of around 5 nm. The consistency between the experiment and simulation is that one can observe the increased red-shift in a wide spectral range using both systems. The decomposition of the fitness function F for ALD and BSA–anti-BSA systems, $|S(\lambda) - S_0(\lambda)|$, for $\lambda = 650\text{--}720 nm is shown in Figure 13. As one can see, the result can be attributed to the$

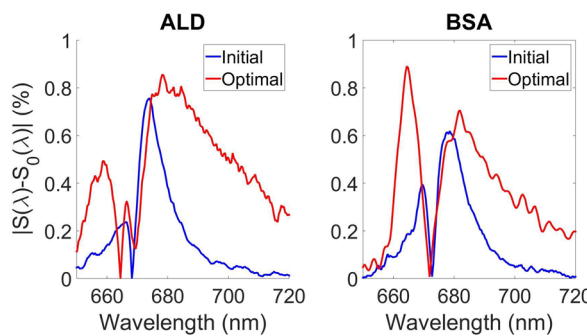


Figure 13. $|S(\lambda) - S_0(\lambda)|$ for ALD and BSA–anti-BSA systems, for $\lambda = 650\text{--}720$ nm.

definition of F based on the SIA since the summation of $|S(\lambda) - S_0(\lambda)|$ is closely correlated to the summation of the wavelength red-shifts over the spectrum. The bandwidth of the SPR lobe is broadened due to the LSPR and geometry variation of every segment, which may result in the perturbations to the consistent resonant response for the initial design. The SIA is the summation of intensity change over the spectrum. In this manner, not only the peak wavelength shift but also red-shifts over a broad band are calculated. Therefore, the optimal design should exhibit enhanced red-shifts over a broad band to achieve a better fitness value. Compared with the conventional design, the red-shift increases in the range of -15 to $+30$ nm as referenced to λ_{SPR} , and one can still observe the enhanced red-shift in the presence of broadened resonances.

CONCLUSION

In conclusion, we propose an optimization for an SPR biosensor using a μ -GA, and the corresponding device is fabricated using the hot embossing nanoimprint technique. The result indicates that the performance of the optimized SPR biosensors can be further improved if more degrees of freedom are enabled for design. The geometry variation in the z -direction results in strong localized SPR at the edges of the nanostructures as well as a perturbation of the transmission spectra. The increase in the fitness value based on SIA is up to 179% and 128% compared with the initial design for FDTD simulations and ALD deposition, respectively. For experimental verification, ALD deposition and BSA and anti-BSA interaction are used, and the results agree well with the simulations. We believe the design concept will benefit the development of various kinds of nanostructure-based SPR biosensors.

METHODS

Hot Embossing Nanoimprint Lithography. The nanostructures are fabricated using the e-beam lithography and reactive-ion etching (RIE) techniques. A layer of PMMA-4A resist is spin-coated onto a silicon substrate with a thickness of 200 nm, and the patterns of nanoslit arrays of $500 \times 500 \mu\text{m}^2$

are written using an e-beam drawing system (Elionix ELS 7,000). The silicon etching is carried out by the following RIE process (Oxford Instrument, Plasmalab 80plus). The flow rates of etching gases CHF_3 and SF_6 are 50 and 25 sccm, respectively. The power of the radio frequency electromagnetic wave and the pressure in the chamber are 150 W and 10^{-2} Torr, respectively. Subsequently, the nanoslit arrays are imprinted onto a COP film using a hot embossing nanoimprint equipment from the silicon substrate, (EHN-3250, Engineering System Co. Ltd.). The gold-capped nanostructures are formed after depositing a gold film on the COP by electron-beam evaporation (AST-Peva-400E).

Optical Setup for Transmission Spectrum Measurement. The optical measurement is demonstrated under a 12 W illumination of a halogen lamp coupled to a fiber cable, where the objective lens of an optical microscope is used for light collimation. The incident polarization is controlled by a linear polarizer, and the light is focused on a capped nanoslit array. The transmitted light is collected by the other objective lens and focused on a fiber cable. The transmission spectra are recorded using a fiber-coupled linear charge-coupled device (CCD) spectrometer (Quest X).

AUTHOR INFORMATION

Corresponding Author

*E-mail: pkwei@sinica.edu.tw.

ORCID

Kuang-Li Lee: 0000-0002-7497-4858

Pei-Kuen Wei: 0000-0002-3002-0526

Author Contributions

P.-H.F. and P.-K.W. performed the simulation and designed the experiments; S.-C.L., P.-C.T., and K.-L.L. did the experiments; P.-H.F. and P.-K.W. cowrote the paper.

Notes

The authors declare no competing financial interest.

ACKNOWLEDGMENTS

This work was supported by the Ministry of Science and Technology (MOST), Taipei, Taiwan, under 106-2112-M-001-006-MY3, 105-2627-B-001-001, 104-2112-M-001-040-MY2, and 103-2221-E-001-013-MY3.

REFERENCES

- (1) Homola, J.; Yee, S. S.; Gauglitz, G. Surface Plasmon Resonance Sensors: Review. *Sens. Actuators, B* **1999**, *54*, 3–15.
- (2) Karlsson, R. SPR for Molecular Interaction Analysis: A Review of Emerging Application Areas. *J. Mol. Recognit.* **2004**, *17*, 151–161.
- (3) Green, R. J.; Frazier, R. A.; Shakesheff, K. M.; Davies, M. C.; Roberts, C. J.; Tendler, S. J. B. Surface plasmon resonance analysis of dynamic biological interactions with biomaterials. *Biomaterials* **2000**, *21*, 1823–1835.
- (4) Roh, S.; Chung, T.; Lee, B. Overview of the Characteristics of Micro- and Nano-Structured Surface Plasmon Resonance Sensors. *Sensors* **2011**, *11*, 1565–1588.
- (5) Brolo, A. G.; Gordon, R.; Leathem, B.; Kavanagh, K. L. Surface Plasmon Sensor Based on the Enhanced Light Transmission through Arrays of Nanoholes in Gold Films. *Langmuir* **2004**, *20*, 4813–4815.
- (6) Tetz, K. A.; Pang, L.; Fainman, Y. High-resolution Surface Plasmon Resonance Sensor Based on Linewidth-optimized Nanohole Array Transmittance. *Opt. Lett.* **2006**, *31*, 1528–1530.
- (7) Henzie, J.; Lee, M. H.; Odom, T. W. Multiscale Patterning of Plasmonic Metamaterials. *Nat. Nanotechnol.* **2007**, *2*, 549.

- (8) Yang, J. C.; Ji, J.; Hogle, J. M.; Larson, D. N. Metallic Nanohole Arrays on Fluoropolymer Substrates as Small Label-Free Real-Time Bioprobes. *Nano Lett.* **2008**, *8*, 2718–2724.
- (9) Lee, K. L.; Huang, J. B.; Chang, J. W.; Wu, S.-H.; Wei, P. K. Ultrasensitive Biosensors Using Enhanced Fano Resonances in Capped Gold Nanoslit Arrays. *Sci. Rep.* **2015**, *5*, 8547.
- (10) Becker, J.; Trügler, A.; Jakab, A.; Hohenester, U.; Sönnichsen, C. The Optimal Aspect Ratio of Gold Nanorods for Plasmonic Biosensing. *Plasmonics* **2010**, *5*, 161–167.
- (11) Nair, S.; Escobedo, C.; Sabat, R. G. Crossed Surface Relief Gratings as Nanoplasmonic Biosensors. *ACS Sensors* **2017**, *2*, 379–385.
- (12) Lesuffleur, A.; Im, H.; Lindquist, N. C.; Oh, S. H. Periodic Nanohole Arrays with Shape-enhanced Plasmon Resonance as Real-time Biosensors. *Appl. Phys. Lett.* **2007**, *90*, 243110.
- (13) Lee, K. L.; Hsu, H. Y.; You, M. L.; Chang, C. C.; Pan, M. Y.; Shi, X.; Ueno, K.; Misawa, H.; Wei, P. K. Highly Sensitive Aluminum-Based Biosensors using Tailorable Fano Resonances in Capped Nanostructures. *Sci. Rep.* **2017**, *7*, 44104.
- (14) Im, H.; Lee, S. H.; Wittenberg, N. J.; Johnson, T. W.; Lindquist, N. C.; Nagpal, P.; Norris, D. J.; Oh, S. H. Template-Stripped Smooth Ag Nanohole Arrays with Silica Shells for Surface Plasmon Resonance Biosensing. *ACS Nano* **2011**, *5*, 6244–6253.
- (15) Bochenkov, V. E.; Frederiksen, M.; Sutherland, D. S. Enhanced Refractive Index Sensitivity of Elevated Short-range Ordered Nanohole Arrays in Optically Thin Plasmonic Au Films. *Opt. Express* **2013**, *21*, 14763–14770.
- (16) Najiminaini, M.; Vasefi, F.; Kaminska, B.; Carson, J. J. L. Effect of Surface Plasmon Energy Matching on the Sensing Capability of Metallic Nano-hole Arrays. *Appl. Phys. Lett.* **2012**, *100*, 063110.
- (17) Bahrami, F.; Aitchison, J. S.; Mojahedi, M. Dual-Wavelength Spectroscopy of a Metallic-Grating-Coupled Surface Plasmon Resonance Biosensor. *IEEE Photonics J.* **2015**, *7*, 1–7.
- (18) Goldberg, D. E. *Genetic Algorithms in Search, Optimization and Machine Learning*; Addison-Wesley Longman Publishing Co., Inc.: Boston, 1989; p 372.
- (19) Håkansson, A.; Sánchez-Dehesa, J. Inverse Designed Photonic Crystal De-multiplex Waveguide Coupler. *Opt. Express* **2005**, *13*, 5440–5449.
- (20) Bahrami, F.; Maisonneuve, M.; Meunier, M.; Aitchison, J. S.; Mojahedi, M. An Improved Refractive Index Sensor Based on Genetic Optimization of Plasmon Waveguide Resonance. *Opt. Express* **2013**, *21*, 20863–20872.
- (21) Fu, P. H.; Tu, Y. C.; Huang, D. W. Broadband Optical Waveguide Couplers with Arbitrary Coupling Ratios Designed Using a Genetic Algorithm. *Opt. Express* **2016**, *24*, 30547–30561.
- (22) Sanchis, L.; Håkansson, A.; López-Zanón, D.; Bravo-Abad, J.; Sánchez-Dehesa, J. Integrated Optical Devices Design by Genetic Algorithm. *Appl. Phys. Lett.* **2004**, *84*, 4460–4462.
- (23) Levi, B.; Richard, J. B. Genetic Algorithm Optimization of Grating Coupled Near-field Interference Lithography Systems at Extreme Numerical Apertures. *J. Opt.* **2017**, *19*, 095003.
- (24) Tehrani, K. F.; Xu, J.; Zhang, Y.; Shen, P.; Kner, P. Adaptive Optics Stochastic Optical Reconstruction Microscopy (AO-STORM) Using a Genetic Algorithm. *Opt. Express* **2015**, *23*, 13677–13692.
- (25) Wang, D.; Zhang, M.; Li, Z.; Song, C.; Fu, M.; Li, J.; Chen, X. System Impairment Compensation in Coherent Optical Communications by Using a Bio-inspired Detector Based on Artificial Neural Network and Genetic Algorithm. *Opt. Commun.* **2017**, *399*, 1–12.
- (26) Shi, C. Z.; Chan, C. C.; Jin, W.; Liao, Y. B.; Zhou, Y.; Demokan, M. S. Improving the Performance of a FBG Sensor network using a genetic algorithm. *Sens. Actuators, A* **2003**, *107*, 57–61.
- (27) Krishnakumar, K. In *Micro-Genetic Algorithms For Stationary And Non-Stationary Function Optimization, 1989 Symposium on Visual Communications, Image Processing, and Intelligent Robotics Systems*; SPIE: Philadelphia, 1990; p 8.
- (28) Lee, K. L.; Chen, P. W.; Wu, S. H.; Huang, J. B.; Yang, S. Y.; Wei, P. K. Enhancing Surface Plasmon Detection Using Template-Stripped Gold Nanoslit Arrays on Plastic Films. *ACS Nano* **2012**, *6*, 2931–2939.
- (29) Johnson, P. B.; Christy, R. W. Optical Constants of the Noble Metals. *Phys. Rev. B* **1972**, *6*, 4370–4379.
- (30) Lee, K. L.; Tsai, P. C.; You, M. L.; Pan, M. Y.; Shi, X.; Ueno, K.; Misawa, H.; Wei, P. K. Enhancing Surface Sensitivity of Nanostructure-Based Aluminum Sensors Using Capped Dielectric Layers. *ACS Omega* **2017**, *2*, 7461–7470.
- (31) Pan, M. Y.; Lee, K. L.; Wang, L.; Wei, P. K. Chip-based Digital Surface Plasmon Resonance Sensing platform for Ultrasensitive Biomolecular Detection. *Biosens. Bioelectron.* **2017**, *91*, 580–587.
- (32) Lee, K. L.; Wei, P. K. Enhancing Surface Plasmon Detection Using Ultrasmall Nanoslits and a Multispectral Integration Method. *Small* **2010**, *6*, 1900–1907.
- (33) Lee, K. L.; You, M. L.; Tsai, C. L.; Hung, C. Y.; Hsieh, S. Y.; Wei, P. K. Visualization of biosensors using enhanced surface plasmon resonances in capped silver nanostructures. *Analyst* **2016**, *141*, 974–980.
- (34) Arwin, H. Optical Properties of Thin Layers of Bovine Serum Albumin, γ -Globulin, and Hemoglobin. *Appl. Spectrosc.* **1986**, *40*, 313–318.
- (35) Sarantopoulou, E.; Petrou, P. S.; Kollia, Z.; Palles, D.; Spyropoulos-Antonakakis, N.; Kakabakos, S.; Cefalas, A.-C. Protein Immobilization and Detection on Laser Processed Polystyrene Surfaces. *J. Appl. Phys.* **2011**, *110*, 064309.